

# **Focal Mechanism Determination of Induced Microearthquakes in an Oil Field Using Full Waveforms from Shallow and Deep Seismic Networks**

Junlun Li, H. Sadi Kuleli, Haijiang Zhang, and M. Nafi Toksoz

Earth Resources Laboratory

Department of Earth, Atmospheric and Planetary Sciences

Massachusetts Institute of Technology

Cambridge, MA 02139

Submitted to Geophysics special issue on induced microseismicity

May 9, 2011

## **Abstract**

A new, high frequency, full waveform matching method is used to study the focal mechanisms of small, local earthquakes induced in an oil field, which are monitored by a sparse near-surface network and a deep borehole network. The determined source properties are helpful for understanding the local stress regime in this field. During the waveform inversion, we maximize both the phase and amplitude matching between the observed and modeled waveforms. We also use the polarities of the first P-wave arrivals and the average S/P amplitude ratios to better constrain the matching. An objective function is constructed to include all four criteria. For different hypocenters and source types, comprehensive synthetic tests show that our method is robust to determine the focal mechanisms under the current array geometries, even when there is considerable velocity inaccuracy. The application to several tens of induced microseismic events showed satisfactory waveform matching between modeled and observed seismograms. The majority of the events have a strike direction parallel with the major NE-SW faults in the region, and some events trend parallel with the NW-SE conjugate faults. The results are consistent with the *in-situ* well breakout measurements and the current knowledge on the stress direction of this region. The source mechanisms of the studied events together with the hypocenter distribution indicate that the microearthquakes are caused by the reactivation of preexisting faults. We observed that the faulting mechanism varies with depth, from strike-slip dominance at shallower depth to normal faulting dominance at greater depth.

## Introduction

Induced seismicity is a common phenomenon in oil/gas reservoirs accompanying changes in internal stress due to water injection or water/oil/gas extraction, etc. (Rutledge & Phillips, 2003; Rutledge et al., 2004; Suckale, 2010; Maxwell et al., 2010). For example, the gas/oil extraction can cause reservoir compaction and reactivate preexisting faults and induce microearthquakes (e.g., Chan & Zoback, 2007; Miyazawa et al., 2008; Sarkar et al., 2008), or injection of water causes the decrease of effective stress and slippage along preexisting faults (Grasso, 1992). The reactivation of preexisting faults is very likely responsible for the sheared casings of production wells in some fields (Maury et al., 1992) or is a serious source of wellbore instability during drillings (Willson et al., 1998; Zoback & Zinke, 2002). Also, the hydraulic fracturing activities in the enhanced geothermal system or in shale gas extraction can result in crack openings and closures and induce microseismicity (Baig & Urbancic, 2010). Through the studying of locations and source characteristics (e.g., focal mechanism) of the induced seismicity over an extended time period, temporal and spatial changes of the stress in the fields may be reconstructed; this can help to understand the intrinsic response of geological formations to the stress disturbance.

Microearthquakes usually have small magnitudes and are generally recorded at sparse local stations. As a result, it is difficult to obtain enough seismic waveforms with high signal to noise ratio for picking the polarity information of first P-wave arrivals. Therefore, it is challenging to use only the P-wave polarity information (even when adding S/P amplitude ratios) as used in conventional methods to constrain the focal mechanisms of the induced earthquakes (e.g., Hardebeck & Shearer, 2002, 2003), especially when there are only a limited number of stations. Waveform matching has been used to determine earthquake focal mechanisms on a

regional and global scale using low frequency waveform information (e.g., Zhao & Helmberger, 1994; Tan & Helmberger, 2007). Zhao & Helmberger (1994) allowed time-shift of synthetic seismogram to account for the imperfect Green's functions when matching with observed seismograms. Tan & Helmberger (2007) matched the direct P-arrival phases (first one cycle after initial P-arrival) between synthetic and observed seismograms in the determination of focal mechanisms. However, in the case of induced seismicity, waveforms usually have higher frequencies. There have been many studies on determining the focal mechanism of the induced seismicity in cases of enhanced geothermal system development, mining and hydraulic fracturing. Godano et al. (2011) used the direct amplitudes of P, SV and SH to study the focal mechanisms of induced microearthquakes in a geothermal site using full-space homogeneous velocity models. Nolen-Hoeksema et al. (2001) used the first half cycle after the first arrivals from the observed seismograms and synthetics from full-space Green's functions to determine the focal mechanisms of several hydraulic fracture events. Julian et al. (2007) used first polarities and amplitude ratios from 16 three-component borehole stations and 14 three-component surface stations to determine the full moment tensors of the induced events and studied the volume change accompanying the geothermal process. High frequency waveform matching, in addition to polarity information, has been used to determine the focal mechanisms of induced earthquakes in a mine with a dense network of 20 stations (Julià et al., 2009). Julià et al. used a full-space homogeneous model to calculate the Green's functions, and they performed the focal mechanism inversion in the frequency domain without phase information in a least square sense between the synthetic and filtered observed data generally below 10 Hz. The simplification to full-space homogeneous model is valid when the receivers are deployed deep in the subsurface and close to the induced events.

To retrieve reliable solutions, we developed a method to use high frequency, full waveform information (both P and S) to determine the focal mechanisms of small earthquakes (Li et al., 2011). Using the known velocity model (one-dimensional layered model in this study), we calculate the Green's functions for all moment tensor components of the source at each location (hypocenter) and then the synthetic seismograms by convolving them with the source time function. To find the best match between the observed and synthetic seismograms, we formulate an objective function that incorporates information from different attributes in the waveforms: the cross correlation values between the modeled waveforms and the data, the  $L_2$  norms of the waveform differences, the polarities of the first P arrivals and the S/P average amplitude ratios. Compared to previous studies, our method uses more attributes of seismograms to better determine the focal mechanisms of induced seismicity. The "high frequency" referred in our study (several Hertz for the shallow network and tens of Hertz for the deep network) is a relative term: it is much higher than the frequency band (0.05-0.5 Hz) often used in the study of large earthquakes (e.g., Tan & Helmberger, 2007), but it is lower than the frequency band often used for exploration seismic imaging (e.g., Etgen et al., 2009). Essentially, the frequency bands used in our study include a considerable portion of the energy radiated from the source, thus the waveforms have good signal-to-noise ratio (SNR) and can reflect the characterizations of the source rupture.

Compared with full waveform tomography or migration techniques, which focus on improving the knowledge of the subsurface structures illuminated by simple active sources with known signatures (e.g., explosion or vibration source with known location and origin time; similar frequency, amplitude, radiation pattern etc. are expected for all shots), the source mechanism determination method takes the velocity model as it is, and focuses on determining

the complicated source signature associated with the events. For induced seismicity in oil and gas fields, the velocity model is generally known from seismics and well logs. Also, comprehensive synthetic tests with random velocity perturbations are performed to examine the robustness of our algorithm in the presence of the velocity uncertainties.

Previously, we tested our newly developed focal mechanism determination method on induced microearthquakes monitored by a five-station surface network at an oil field in Oman (Li et al., 2011). The field, operated by Petroleum Development Oman (PDO), was discovered in 1962 and put into production in 1969. An official program to monitor induced seismicity using a surface station network in the field commenced in 1999 and a borehole network was installed in February of 2002. The primary objective of this passive seismicity monitoring program was to locate the events and to correlate them with production and injection activities in order to understand and monitor the cause of induced seismicity in the field. In this paper, we applied the newly developed focal mechanism determination method to data from the borehole network. The source mechanisms determined using the borehole network are compared to those determined using the surface network. The robustness of the method is tested extensively on synthetic datasets generated for both the surface and borehole networks using a randomly perturbed velocity model.

### **Induced Microearthquake Dataset**

The petroleum field discussed in this paper is a large anticline created by deep-seated salt movement (Sarkar, 2008). The dome is about  $15 \times 20$  km in size with a northeast-southwest axial elongation that is probably a result of regional deformation. The structure is dominated by a major central graben and two systems of faulting with two preferred directions (southeast-

northwest and northeast-southwest) that affect the trapping mechanism in the oil reservoir. The northeast-southwest major network of faults and fractures partially connects all parts of the fields together (Figures 1, 2). The main oil production is from the Lower Cretaceous Shuaiba chalk overlain unconformably by Nahr Umr shale, while gas is produced from the shallower Natih Formation overlain by the Fiqa shale Formation (Sarkar, 2008; Zhang et al., 2009).

Since 1996, increasing seismic activity has been reported by the staff working in the field. Significant surface subsidence in the center of the field has also been observed by InSAR, GPS and leveling surveys, and has been attributed to compaction of the Natih formation (Bourne et al., 2006). To monitor the induced seismicity in the field, PDO first deployed a surface array of monitoring stations in 1999 (Figure 1). The stations are instrumented with SM-6B geophones with a natural frequency ( $f_n$ ) of 4.5 Hz. In 2002, another network, independent of the shallow network, was installed in the field as part of a Shell/PDO collaborative study (Figure 2). Unlike the surface array/shallow network, this network had borehole installations of seismic sensors (SM-7m,  $f_n=30$  Hz) at multiple levels, roughly ranging from depths 750 m – 1250 m. The instrumentation for this network was much deeper than that of the surface network and, therefore, this monitoring network is referred to as the “borehole network.” A schematic diagram of the wells and sensor positions is shown in Figure 2. The borehole network consisted of 5 closely spaced monitoring wells in the most seismically active part of the reservoir and covered a much smaller area than the surface network. Due to sensor positions at depths, the ability to acquire data at much higher frequencies and the proximity to the two producing units (Natih gas and Shuaiba oil), the deep network recorded much smaller magnitude events than the shallow network, resulting in a greatly increased detectability of induced seismicity (roughly about 25 times more induced events per day) compared to the shallow network. The borehole network was

operational for about 18 months starting in February 2002; however, only microseismic data from the last 11 months (October 2002 – August 2003) were available for this study. During that 11 month monitoring period, about 15,800 events were identified with an average rate of  $\sim 47/\text{day}$ , out of which we analyzed and located about 5,400 events (Sarkar, 2008). Attempts were made to select common events detected during this period by both (deep and shallow) networks for a joint location analysis, however, due to clock synchronization problems and difference in sensor frequency bands between the two networks, the common events could not be identified, and hence the task could not be accomplished. Some research indicated that by carefully identifying the largest events in different networks, synchronization between networks sometimes can be achieved by shifting the origin times in one network with a constant time (Eisner et al., 2010). The similar strategy will be adopted in the future.

During the period of 1999 to 2007, over 1500 induced earthquakes were recorded by the surface network, and their occurrence frequency was found to be correlated with the amount of gas production (Sarkar, 2008). The distribution of induced events in the field recorded by the surface network is shown in Figure 1 (Sarkar, 2008; Sarkar et al., 2008; Zhang et al., 2009). All the events have a residual traveltimes of less than 30 ms, indicating they are well located. Figure 2 shows the microearthquake locations determined using the deep borehole network and the double-difference tomography method (Zhang et al., 2009). The root-mean-square travel time residual is around 10 ms (Zhang et al., 2009). In the map view, the earthquakes are mainly distributed along the mapped two NE-SW fault systems, although there are also some earthquakes distributed along the conjugate NW-SE fault system. This earthquake distribution suggests that most of the earthquakes are induced by the reactivation of the existing faults in the field. Figure 3 and Figure 4 show typical events and their spectrograms recorded by the surface



network and borehole network, respectively. Because of the proximity of the earthquake source to the deep borehole network, the frequency content of the recorded waveform by the borehole network is much higher than by the surface network. For the waveforms recorded by the surface network, there is a considerable amount of energy in the frequency range of 3 to 9 Hz (Figure 3). For the deep borehole network, the recorded waveforms contain significant energy between 15 to 35 Hz (Figure 4).

### **Focal Mechanism Determination Method**

A detailed description of the method can be found in Li et al. (2011). Here the method is briefly explained. The focal mechanism can be represented by a 3 by 3 second order moment tensor with six independent components (Aki & Richards, 2003). Here we assume the focal mechanism of the small induced events can be represented by pure double couples (Rutledge & Phillips, 2002), though it is possible that a volume change or Compensated Linear Vector Dipoles (CLVD) part may also exist, especially in hydraulic fracturing cases, and the non-double-couple components are informative for understanding the rock failure under high-pressure fluid (Ross & Foulger, 1996; Jechumtálová & Eisner, 2008; Šílený et al., 2009; Song & Toksoz, 2010). The constraining of focal mechanism as double couple (DC) can eliminate the spurious non-DC components in the inversion raised by modeling the wave propagation in anisotropic medium with isotropic Green's functions or inaccuracy of the velocity model (Šílený & Vavryčuk, 2002; Godano et al., 2011). However, if strong non-DC components actually exist in the source rupture process, the determined fault plane may be biased (e.g., Jechumtálová & Šílený, 2001; Jechumtálová & Šílený, 2005). In our analysis, we describe the DC focal mechanism of seismic source in terms of its strike ( $\Phi$ ), dip ( $\delta$ ) and rake ( $\lambda$ ), and determine

double couple components from these three parameters. The simplification of the source is supported by the observation that almost all the detected microearthquakes occurred along preexisting faults, i.e., reactivated faults slipping along preexisting weak zones would not cause significant volumetric or CLVD components (Julian et al., 1998). For each component of a moment tensor, we use the Discrete Wavenumber Method (DWN) (Bouchon, 1981, 2003) to calculate its Green's functions  $G_{ij,k}^n(t)$  for the horizontally layered medium. It should be noted that if the full moment tensor needs to be determined, e.g., in the hydraulic fracturing cases, the seismic source should be described with six independent tensor components, which will increase the cost in searching the best solution. The structure between the earthquake and the station is represented as a 1-D horizontally layered medium, which can be built from 1) averaging borehole sonic logs across this region, or 2) extracting the velocity structure between the source and the receiver from the 3-D velocity model from double-difference seismic tomography for passive seismic events (Zhang et al., 2009).

The modeled waveform from a certain combination of strike, dip, and rake is expressed as a linear combination of weighted Green's functions:

$$V_i^n = \sum_{j=1}^3 \sum_{k=1}^3 m_{jk} G_{ij,k}^n(t) * s(t) \quad (1)$$

where  $V_i^n$  is the modeled  $i^{\text{th}}$  (north, east or vertical) component at station  $n$ ;  $m_{jk}$  is the moment tensor component and is determined by the data from all stations;  $G_{ij,k}^n(t)$  is the  $i^{\text{th}}$  component of the Green's functions for the  $(j, k)$  entry at station  $n$ , and  $s(t)$  is the source time function. In this study, a smooth ramp is used for  $s(t)$ , the duration of which can be estimated from the spectra of the recorded seismograms (Bouchon, 1981). The source time functions are found to be

insensitive to the waveform fitting, as both the synthetic and observed seismograms are low-pass filtered before comparisons (Zhao et al., 2006). Using reciprocity by strain Green's tensors can improve the efficiency of calculating the Green's functions, especially when the sources greatly outnumber the stations (Eisner & Clayton, 2001; Zhao et al., 2006). For instance, only one numerical simulation with reciprocity (e.g., finite difference method), by setting a source at a station, is needed to calculate the Green's functions for all six components of the moment tensor between anywhere in the field and one component at the station in a 3-D heterogeneous medium.

Earthquake locations are usually provided by the traveltime location method. However, due to uncertainties in velocity model and arrival times, the seismic event locations may have errors, especially in focal depth determined from the surface network. While matching the modeled and observed waveforms, we also search for an improved location  $(x, y, z)$  around the catalog location.

To determine the best solution, we construct an objective function that characterizes the similarity between the modeled and observed waveforms. We use the following objective function, which evaluates four different aspects of the waveform information:

$$\begin{aligned} \text{maximize}(J(x, y, z, \Phi, \delta, \lambda, t_s)) = & \\ \sum_{n=1}^N \sum_{j=1}^3 \{ & \alpha_1 \max(\tilde{d}_j^n \otimes \tilde{v}_j^n) - \alpha_2 \|\tilde{d}_j^n - \tilde{v}_j^n\|_2 \\ & + \alpha_3 f(\text{pol}(\tilde{d}_j^n), \text{pol}(\tilde{v}_j^n)) + \alpha_4 h(\text{rat}(\frac{S(d_j^n)}{P(d_j^n)}, \text{rat}(\frac{S(v_j^n)}{P(v_j^n)}))\} \end{aligned} \quad (2)$$

Here  $\tilde{d}_j^n$  is the normalized data and  $\tilde{v}_j^n$  is the normalized modeled waveform.  $x, y, z$  are the event hypocenter that will be re-determined by waveform matching;  $t_s$  is the time shift which gives the largest cross correlation value between the observed and synthetic seismograms (1<sup>st</sup>

term). Since it is difficult to obtain accurate absolute amplitudes due to site effects in many situations, we normalize the filtered observed and modeled waveforms before comparison. The normalization used here is the energy normalization, such that the energy of the normalized wave train within a time window adds to unity. Compared to peak amplitude normalization, energy normalization is less affected by site effects which may cause abnormally large peaks due to focusing and other factors. In a concise form, this normalization can be written as:

$$\tilde{d}_j^n = \frac{d_j^n}{\sqrt{\int_{t_1}^{t_2} (d_j^n)^2 dt}} \quad (3)$$

where  $t_1$  and  $t_2$  are the boundaries of the time window.

The objective function  $J$  in Equation 2 consists of 4 terms.  $\alpha_1$  through  $\alpha_4$  are the weights for each term. Each weight is a positive scalar number and is optimally chosen in a way such that no single term will over-dominate the objective function. We used  $\alpha_1=3$ ,  $\alpha_2=3$ ,  $\alpha_3=1$  and  $\alpha_4=0.5$  for the synthetic tests and real events. The first term in Equation 2 evaluates the maximum cross correlation between the normalized data ( $\tilde{d}_j^n$ ) and the normalized modeled waveforms ( $\tilde{v}_j^n$ ). From the cross-correlation, we find the time-shift ( $t_s$ ) to align the modeled waveform with the observed waveform. The second term evaluates the  $L_2$  norm of the direct differences between the aligned modeled and observed waveforms (note the minus sign of the 2<sup>nd</sup> term in order to minimize the amplitude differences). The first two terms are not independent of each other, however, they have different sensitivities at different frequency bands and by combining them together the waveform similarity can be better characterized. The third term evaluates whether the polarities of the first P-wave arrivals as observed in the data are consistent with those in the modeled waveforms.  $pol$  is a weighted sign function which can be  $\{\beta, -\beta, 0\}$ , where  $\beta$  is a

weight reflecting our confidence in picking the polarities of the first P-wave arrivals in the observed data. Zero (0) means undetermined polarity.  $f$  is a function that penalizes the polarity sign inconsistency in such a way that the polarity consistency gives a positive value while polarity inconsistency gives a negative value. The matching of the first P-wave polarities between modeled and observed waveforms is an important condition for determining the focal mechanism, when the polarities can be clearly identified. Polarity consistency at some stations can be violated if the polarity is not confidently identified (small  $\beta$ ) and the other three terms favor a certain focal mechanism. Therefore, the polarity information is incorporated into our objective function with some flexibility. By summing over the waveforms in a narrow window around the arrival time and checking the sign of the summation, we determine the polarities robustly for the modeled data. For the observed data, we determine the P-wave polarities manually.

The fourth term in the objective function is to evaluate the consistency of the average S/P amplitude ratios in the observed and modeled waveforms (Hardebeck & Shearer, 2003). The “ $rat$ ” is the ratio evaluation function and it can be written as:

$$rat = \frac{\int_{T_2}^{T_3} |r_j^n(t)| dt}{\int_{T_1}^{T_2} |r_j^n(t)| dt} \quad (4)$$

where  $[T_1 T_2]$  and  $[T_2 T_3]$  define the time window of P- and S-waves, respectively, and  $r_j^n$  denotes either  $d_j^n$  or  $v_j^n$ . The term  $h$  is a function which penalizes the ratio differences so that the better matching gives a higher value. Note that here we use the un-normalized waveforms  $d_j^n$  and  $v_j^n$ .

In general, the amplitudes of P-waves are much smaller than those of S-waves. To balance the contribution between P- and S-waves, we need to fit P- and S-waves separately using the first two terms in Equation 2. Also, by separating S- from P-waves and allowing an independent time-shift in comparing observed data with modeled waveforms, it is helpful to deal with incorrect phase arrival time due to incorrect  $V_p/V_s$  ratios (Zhu & Helmberger, 1996). Here we allow independent shifts for different stations as well as for P- and S-waves. We calculate both the first P- and S-arrival times by the finite difference Eikonal solver (Podvin & Lecomte, 1991). The wave train is then separated into two parts at the beginning of the S-wave. The window for the P-wave comparison is from the first arrival to the beginning of the S-wave, and the window for the S-wave comparison is proportional to the epicenter distance. It should be noted that the full wave train is not included as later arrivals, usually due to scattering from heterogeneous media, cause larger inaccuracies in waveform modeling.

In some cases, when we have more confidence in some stations, e.g., stations with short epicenter distance, or stations deployed on known simpler velocity structure, we can give more weight to those stations by multiplying  $\alpha_1$ -  $\alpha_4$  with an additional station weight factor.

The comparison algorithm (Equation 2) is optimized such that it can be performed on a multicore desktop machine usually within 10 minutes, even when several millions of synthetic traces are compared with the data. The computation of the Green's function library using DWN takes more time, but it only needs to be computed once.

The passive seismic tomography only provides a detailed 3-D velocity model close to the central area of the field due to the earthquake-station geometry (Zhang et al., 2009). Therefore, for the focal mechanism determination through the surface network, of which most stations are not placed within the central area (Figure 1), we use the 1-D layered velocity model from the

averaged sonic logs (Sarkar, 2008; Zhang et al., 2009). Considering that we use a frequency band of 3-9 Hz (Figure 3) in our waveform matching for this surface network, corresponding to a dominant P-wave wavelength of 800 m and S-wave wavelength of 400 m, the velocity model should satisfy our modeling requirement. The deep network consists of five boreholes with eight-level of receivers at different depths in each borehole (Figure 2). Due to the proximity of borehole receivers to the seismicity, we were able to record the seismograms of very small induced seismicity. Waveforms between 15-35 Hz are used to determine the focal mechanisms (Figure 4). To better model the waveforms, we replaced part of the 1-D average layered velocity model with the extracted P- and S-wave velocities from the 3-D tomographic model between 0.7 km and 1.2 km in depth, where it has the highest resolution and reliability. Note that the updated 1-D velocity model between the earthquake and each station becomes different for the deep borehole network.

### **Synthetic Tests for the Surface and Deep Borehole Networks**

In Li et al. (2011), we tested the robustness of the method on the surface network. To account for the uncertainty of the 1-D velocity model, a 5% random perturbation was applied. Here we consider a greater uncertainty in the velocity model -up to 8%- and test more cases for different focal mechanisms and event locations. We first use the station configuration of the surface network in our test, as it provides a considerable challenge due to the large epicenter distance and the relative inaccuracy in the computation of Green's functions by using the 1-D averaged velocity model from several sonic logs. We choose three different epicenters (E1, E2 and E3), and for each epicenter we choose three different depths (D1=1000 m, D2=1200 m and D3=1700 m), corresponding to shallow, medium and deep events in this field, respectively. At

each depth, we test three different focal mechanisms, which yield 27 different synthetic tests in total. The different focal mechanisms and widely distributed hypocenters in the synthetic test give a comprehensive robustness test for the focal mechanism determination in this region. The station configuration and the hypocenter distribution are shown in Figure 1. At each hypocenter, three distinct mechanisms are tested, namely M1:  $\Phi=210^\circ$ ,  $\delta=50^\circ$ ,  $\lambda=-40^\circ$ ; M2:  $\Phi=50^\circ$ ,  $\delta=60^\circ$ ,  $\lambda=-70^\circ$ ; and M3:  $\Phi=130^\circ$ ,  $\delta=80^\circ$ ,  $\lambda=80^\circ$  (Table 1). Three or four first P-arrival polarities are used in each synthetic test, resembling the measurements we have for real data for this surface network. In real cases, as inevitable differences exist between the derived velocity model and the true velocity model, we need to examine the robustness of our method under such circumstances. We add up to 8% of the layer's velocity as the random velocity perturbation to the reference velocity model in each layer (Figure 5) and use the perturbed velocity models to generate synthetic data. The perturbation is independent for five stations, i.e., the velocity model is path-dependent and varies among different event-station pairs to reflect the 3-D velocity heterogeneities in the field. Also, the perturbation is independent for the P-wave and S-wave velocities in a specific velocity model for an event-station pair. The Green's functions (modeled data) are generated with the reference velocity model. Figure 6 shows the modeled seismograms with offset using the reference velocity model. The predicted traveltimes by the eikonal equation and the first arrivals in the waveforms are matched well. It should also be noted that the P-wave and S-wave velocity perturbation from one station to another can reach up to 800 m/s in some layers. Considering that this reservoir consists mainly of sedimentary rocks, the magnitude of the random lateral velocity perturbation should reflect the upper bounds of the local lateral velocity inhomogeneity. The density is not perturbed in this test, as the velocity perturbation is dominant in determining the characteristics of the waveforms. Also, the layer thickness is not perturbed, as



perturbation in either layer velocity or thickness generates equivalent phase distortions from each layer. The test results are summarized in Table 1. Although the perturbation can change the waveform characteristics to a very large extent, the synthetic test shows that our method can still find a solution very close to the correct one by including information from different aspects of the waveforms, even when only records from five vertical components are used. Figure 7 shows a waveform match between the synthetic data and the modeled data. The best solution found is (230°, 60°, -40°), close to the correct solution (210°, 50°, -40°) in comparison. The synthetic event is at 1220 m in depth.

In general, the focal mechanisms are reliably recovered (Table 1). To quantify the recoverability, we define the mean recovery error for the focal parameters:

$$\Delta\varphi_m^e = \frac{\sum_{d=1}^3 |\varphi_{m,d}^e - \varphi_m|}{3} \quad (7)$$

where  $\varphi_{m,d}^e$  is the recovered strike, dip or rake for epicenter  $e$ , with mechanism  $m$  at depth  $d$ , where  $e, m, d \in \{1, 2, 3\}$ , and  $\varphi_m$  is the reference (true) focal parameter for mechanism  $m$ . It is found that  $\Delta\varphi$  is only a weak function of epicenter, with marginally smaller value for E1 than for E2 or E3 in general. Also, we found that for each individual depth  $\Delta\varphi$  ( $d=1, 2$  or  $3$ ) is marginally smaller for shallower earthquakes (D1 and D2) than for deeper earthquakes (D3) (results not tabulated). Due to our use of only vertical components, we found that the uncertainty in strike is slightly larger than that in dip or rake. In general, no distinct variation of  $\Delta\varphi$  is found against the hypocenter or faulting type. Therefore, we conclude that our method is not very sensitive to the faulting type, to the azimuthal coverage of the stations, or to the hypocenter position within a reasonable range for the array geometries studied.

For the borehole network, we perform a similar synthetic test to check the reliability of our method for the deep network configuration. As we have shown that the reliability of our method is not very sensitive to the azimuthal coverage of the stations or to the depth of the event in a reasonable range, we only perform synthetic experiments at two hypocenters with three different mechanisms, respectively, for the deep borehole network (Table 2). Nine to eleven receivers are used for each case. The frequency band is the same as we use for the real data set (15 – 35 Hz). A typical waveform comparison for the synthetic test is shown in Figure 8. It is also found that the method is robust with the borehole receiver configuration using higher frequency seismograms.

### **Application to Field Data**

We applied this method to study 40 microearthquakes using surface and deep borehole networks. The instrumental responses have been removed before processing. An attenuation model with Q value increasing with depth (Table 3) was used for the waveform modeling. In general, we consider the attenuation larger (smaller Q) close to the surface due to weathering, and the attenuation for S-waves larger than for P-waves at the same depth. Figure 9 shows the beachballs of the nine best solutions out of millions of trials for a typical event recorded by the surface network. Our best solution (the one at the bottom right, reverse strike-slip) has a strike of  $325^\circ$ , which is quite close to the best known orientation  $320^\circ$  of the NW-SE conjugate fault (Figure 1). Figure 10 shows the comparison between the modeled and the observed data for this event. The waveform similarity between the modeled and observed data is good. Typically, the cross correlation coefficient is greater than 0.7. Additionally, the S/P waveform amplitude ratios in the modeled and observed data are quite close, and the first P arrival polarities are identical in

the modeled and observed data for each station. In this example, all four criteria in Equation (2) are evaluated, and they are consistent between the modeled and observed data.

For the deep borehole network, we use the frequency band 15~35 Hz, which includes enough energy in the spectra to provide good SNR, for determining the focal mechanisms of these small magnitude earthquakes from the borehole network data (Figure 4). As there is also uncertainty in the orientations of the horizontal components, we use only the vertical components of the 4-C sensors configured in a proprietary tetrahedral shape for each level (Jones, et al., 2004). Although there are in total 40 vertical receivers, we often only use about 10 seismograms in determining each event due to the following reasons:

- 1) Some receivers are only separated by ~30 m vertically and therefore do not provide much additional information for determining the source mechanism;

- 2) Some traces show peculiar, unexplainable characteristics in seismograms and are, therefore, discarded. Also, the SNR for some traces is very poor.

In our selection of seismograms, we try to include data from different wells to provide a better azimuthal coverage, as well as from different depths spanning a large vertical range, providing waveform samplings at various radiation directions of the source.

Figure 11 shows the comparison between the observed and modeled seismograms for a typical event recorded by the deep borehole network. Eleven receivers from four boreholes are used in this determination. Among the eleven seismograms, five first P-wave arrival polarities are identified and then used in this determination. The waveform similarities, average S/P amplitude ratio and consistency in the P-wave arrival polarities are satisfactory. Comparing Figure 11 with Figure 10, we found the fewer matched cycles in the deep borehole case. Similar comparison can also be found between the shallow and deep borehole synthetic tests (Figures 7

and 8), where focal mechanisms close to the correct solutions were still found in both synthetic cases.

Using this method, we have studied 40 earthquakes distributed across this oil field from both the surface network and the borehole network. Among these studied events, 22 events are recorded by the surface network, 18 events are from the borehole network. Figure 12 shows that the majority of the events primarily have the normal faulting mechanism, while some have the strike-slip mechanism, and some have a reverse faulting mechanism. The strike directions of most events are found to be approximately parallel with the NE trending fault, suggesting the correlation of these events with the NE trending fault. However, some events also have their strikes in the direction of the conjugate NW trending fault, suggesting that the reactivation also occurred on the conjugate faults. Although the number of studied events is small compared to the total recorded events, their mechanisms still provide us with some insights on the fault reactivation in this field: 1) The hypocenter distribution and the determined source mechanisms (e.g., strikes) indicate that the reactivation of preexisting faults is the main cause of the induced microearthquakes in this field, and both the NE trending fault and its conjugate fault trending in the NW direction are still active. Interestingly, we note that the strike directions of the normal faulting events (red) are slightly rotated counterclockwise with respect to the mapped fault traces from the 3-D active seismic data and are consistent with the trend of the located earthquake locations (Figure 1, 2). The counterclockwise rotation may be due to the non-planar geometry of the fault, i.e., the strike of the shallow part of the fault as delineated by the surface seismic survey does not need to be the same as the deeper part of the fault, where most induced seismicity is located; 2) Most strike-slip events (Cyan) are shallow, suggesting that the maximum horizontal stress ( $S_{Hmax}$ ) is still larger than the vertical stress ( $S_v$ ) at this depth range. However,

deeper events (e.g., red, blue) mainly have a normal faulting mechanism, suggesting  $S_v$  exceeds  $S_{Hmax}$  when depth increases beyond ~1km in this region. The dominance of normal faulting is consistent with the study by Zoback et al. (2002) on the Valhall and Ekofisk oil fields, where reservoir depletion induced normal faulting in and above the productive horizon. In this oil field, most induced earthquakes occurred above the oil layer, which is located around 1.5 km below the surface. 3) Assuming  $S_{Hmax}$  is parallel with the strike of normal faulting events, perpendicular to the strike of reverse events, and bisects the two fault planes of the strike-slip events (Zoback, 2007), the majority of the determined events then suggest a  $S_{Hmax}$  trending NE or NNE, which is consistent with the well breakout measurement and local tectonic stress analysis in the region (Al-Anboori, 2005). The observations indicate that the regional preexisting horizontal stress and the vertical stress played an important role in the reactivation of these preexisting faults.

## Conclusions

In this study, we used our recently developed high-frequency waveform matching method to determine the microearthquakes in an oil field with the surface and borehole network data. This method is especially applicable to the study of microearthquakes recorded by a small number of stations, even when some first P arrival polarities are not identifiable due to noise contamination, or only the vertical components are usable. The objective function, formulated to include matching phase and amplitude information, first arrival P polarities and S/P amplitude ratios between the modeled and observed waveforms, yields reliable solutions. We also performed systematic synthetic tests to verify the stability of our method.

For the 40 studied events, we found that the hypocenters and strikes of the events are correlated with preexisting faults, indicating that the microearthquakes occur primarily by

reactivation of the preexisting faults. We also found that the maximum horizontal stress derived from the source mechanisms trends in the NE or NNE direction; this is consistent with the direction of the maximum horizontal stress obtained from well breakout measurements and local tectonic stress analysis. Our investigation shows that the study of the source mechanisms of the induced microearthquakes can provide insights into the local stress heterogeneity and help to better understand the induced microearthquakes by oil or gas production.

### **Acknowledgement**

The work presented here was partly supported by the Department of Energy under grant DE-FG3608GO18190. J. Li is grateful for the financial support by the MIT-Kuwait center, and the authors want to thank Petroleum Development Oman (PDO) for providing the data and support for this study.

## References

- Aki, K. and P. Richards, 2002, Quantitative Seismology, 2<sup>nd</sup> Edition: University Science Books.
- Al-Anboori, A.S.S., 2005, Anisotropy, focal mechanisms, and state of stress in an oilfield: Passive seismic monitoring in Oman: Ph.D. thesis, the university of Leeds.
- Baig, A. and T. Urbancic, 2010, Microseismic moment tensors: a path to understanding frac growth: the Leading Edge, 320-324.
- Bouchon, M., 1981, A simple method to calculate Green's functions for elastic layered media: Bulletin of the Seismological Society of America, **71**, 959-971.
- Bouchon, M., 2003, A review of the discrete wavenumber method: Pure and Applied Geophysics, **160**, 445-465.
- Bourne, S.J., K. Maron, S.J. Oates, and G. Mueller, 2006, Monitoring Reservoir Deformation on Land - Evidence for Fault Re-Activation from Microseismic, InSAR, and GPS Data: 68<sup>th</sup> EAGE Conference, EAGE Extended Abstract.
- Chan, A.W. and M.D. Zoback, 2007, The role of hydrocarbon production on land subsidence and fault reactivation in the Louisiana coastal zone: Journal of Coastal Research, **23**, 771-786.
- Dreger, D., R. Uhrhammer, M. Pasyanos, J. Franck and B. Romanowicz, 1998, Regional and far-regional earthquake locations and source parameters using sparse broadband networks: a test on the Ridgecrest sequence: Bulletin of the Seismological Society of America, **88**, 1353-1362.
- Eisner L. and R.W. Clayton, 2001, A reciprocity method for multiple-source simulations: Bulletin of the Seismological Society of America, **91** (3), 553-560.

- Eisner, L, B. J. Hulsey, P. Duncan, D. Jurick, H. Werner, W. Keller. 2010: Comparison of surface and borehole locations of induced microseismicity. *Geophysical Prospecting*, 58, 5, pp. 809-820; doi: 10.1111/j.1365-2478.2010.00867.x
- Etgen J., S.H. Gray and Y. Zhang, 2009, An overview of depth imaging in exploration geophysics: *Geophysics*, **74**, WCA5-WCA17.
- Godano, M., T. Bardainne, M. Regnier and A. Deschamps, 2011, Moment-tensor determination by nonlinear inversion of amplitudes: *Bulletin of the Seismological Society of America*, **101**, 366-378.
- Grasso J.R., 1992, Mechanics of seismic instabilities induced by the recovery of hydrocarbons: *Pure and Applied Geophysics*, **139**, 507-534.
- Hardebeck, J.L. and P.M. Shearer, 2002, A new method for determining first-motion focal mechanisms: *Bulletin of the Seismological Society of America*, **93**, 1875-1889.
- Hardebeck, J.L. and P.M. Shearer, 2003, Using S/P amplitude ratios to constrain the focal mechanisms of small earthquakes: *Bulletin of the Seismological Society of America*, **93**, 2434-2444.
- Jechumtálová, Z., J. Šílený, 2001, Point-source parameters from noisy waveforms: error estimate by Monte Carlo simulation: *Pure and Applied Geophysics*, **158**, 1639–1654.
- Jechumtálová, Z., J. Šílený, 2005, Amplitude ratios for complete moment tensor retrieval: *Geophysical Research Letters*, **32**, L22303.
- Jechumtálová, Z. and Eisner, L., 2008, Seismic source mechanism inversion from a linear array of receivers reveals non-double-couple seismic events induced by hydraulic fracturing in sedimentary formation. *Tectonophysics*, 460 (1-4), 124-133.



- Jones, R.H., D. Raymer, G. Mueller, H. Rynja, and K. Maron, 2004, Microseismic Monitoring of the Yibal Oilfield, : 66<sup>th</sup> EAGE Conference, EAGE Extended Abstract.
- Julian, B.R., A.D. Miller and G.R. Foulger, 1998, Non-double-couple earthquakes, 1. Theory: Reviews of Geophysics, **36**, 525-549.
- Julian, B.R., G.R. Foulger, and F. Monastero, 2007, Microearthquake moment tensors from the Coso Geothermal area, in Proceedings, Thirty-Second Workshop on Geothermal Reservoir Engineering, Paper SGP-TR-183, Stanford Univ., Stanford, Calif.
- Julià, J. and A.A. Nyblade, 2009, Source mechanisms of mine-related seismicity, Savuka mine, South Africa: Bulletin of the Seismological Society of America, **99**, 2801-2814.
- Li, J., H. Zhang, H.S. Kuleli, and M.N. Toksoz, 2011, Focal mechanism determination using high-frequency waveform matching and its application to small magnitude induced earthquakes: Geophysical Journal International, no. doi: 10.1111/j.1365-246X.2010.04903.x.
- Maury V.M.R., J. R. Grasso and G. Wittlinger, 1992, Monitoring of subsidence and induced seismicity in the Larq gas field (France): the consequences on gas production and field operation: Engineering Geology, **32**, 123-135.
- Maxwell, S.C., J. Rutledge, R. Jones, and M. Fehler, 2010, Petroleum reservoir characterization using downhole microseismic monitoring: Geophysics, **75**, 75A129–75A137.
- Miyazawa, M., A. Venkataraman, R. Snieder, and M.A. Payne, 2008, Analysis of microearthquake data at Cold Lake and its applications to reservoir monitoring: Geophysics, **73**, O15-O21.
- Muller, G., 1985, The reflectivity method: a tutorial: Journal of Geophysics, **58**, 153-174.

- Nolen-Hoeksema, R. C., and L. J. Ruff (2001), Moment tensor inversion of microseisms from the B-sand propped hydrofracture, M-site, Colorado, *Tectonophysics*, 336, 163– 181, doi:10.1016/S0040-1951(01)00100-7.
- Podvin, P. and I. Lecomte, 1991, Finite difference computation of traveltimes in very contrasted velocity models: a massively parallel approach and its associated tools: *Geophysical Journal International*, **105**, 271-284.
- Ross A. and G.R. Foulger, 1996, Non-double-couple earthquake mechanism at the Geysers geothermal area, California, *Geophysical Research Letters*, **23**, 877-880.
- Rutledge, J.T. and W.S. Phillips, 2002, A comparison of microseismicity induced by gel-proppant and water-injected hydraulic fractures, Carthage Cotton Valley gas field, East Texas: 72nd Annual International Meeting, SEG, Expanded Abstracts, 2393-2396.
- Rutledge, J.T. and W.S. Phillips, 2003, Hydraulic stimulation of natural fractures as revealed by induced microearthquakes, Carthage Cotton Valley gas field, east Texas: *Geophysics*, **68**, 441-452.
- Rutledge, J.T., W.S. Phillips and M.J. Mayerhofer, 2004, Faulting induced by forced fluid injection and fluid flow forced by faulting: and interpretation of hydraulic-fracture microseismicity, Carthage Cotton Valley gas field, Texas: *Bulletin of the Seismological Society of America*, **94**, 1817-1830.
- Sarkar, S., 2008, Reservoir monitoring using induced seismicity at a petroleum field in Oman: PhD thesis, Massachusetts Institute of Technology, Cambridge, Massachusetts, US.
- Sarkar, S., H.S. Kuleli, M.N. Toksoz, H. Zhang, O. Ibi, F. Al-Kindy and N. Al Touqi, 2008, Eight years of passive seismic monitoring at a petroleum field in Oman: a case study: 78<sup>th</sup> Annual International Meeting, SEG, Expanded Abstracts, 1397-1401.

- Šílený, J., and V. Vavryčuk, 2002, Can unbiased source be retrieved from anisotropic waveforms by using an isotropic model of the medium?: *Tectonophysics*, **356**, 125-138.
- Šílený, J., D. P. Hill, L. Eisner, and F. H. Cornet, 2009, Non-double-couple mechanisms of microearthquakes induced by hydraulic fracturing, *Journal of Geophysical Research*, **114**, B08307, doi:10.1029/2008JB005987
- Song, F. and M.N. Toksoz, 2010, Downhole microseismic monitoring of hydraulic fracturing: a full-waveform approach for complete moment tensor inversion and stress estimation, Presented at 2010 SEG microseismicity workshop, Denver, CO.
- Suckale, J., 2010, Induced seismicity in hydrocarbon fields: Chapter 2, *advances in Geophysics*, **51**.
- Tan, Y. and D.V. Helmberger, 2007, A new method for determining small earthquake source parameters using short-period P waves: *Bulletin of the Seismological Society of America*, **97**, 1176-1195.
- Willson, S., N.C. Last, M.D. Zoback and D. Moos, 1998, Drilling in South America: a wellbore stability approach for complex geologic conditions: SPE 53940, in 1999 SPE Latin American and Caribbean petroleum engineering conference, Caracas, Venezuela 21-23, April, 1999.
- Zhang, H.J., S. Sarkar, M.N. Toksoz, H.S. Kuleli and F. Al-Kindy, 2009, Passive seismic tomography using induced seismicity at a petroleum field in Oman: *Geophysics*, **74**, WCB57-WCB69.
- Zhao, L., P. Chen and T.H. Jordan, 2006, Strain Green's Tensors, Reciprocity and Their Applications to Seismic Source and Structure Studies: *Bulletin of the Seismological Society of America*, **96**, 1753-1763.

- Zhao L.S. and D.V. Helmberger, 1994, Source estimation from broadband regional seismograms, Bulletin of the Seismological Society of America, **84**, 91-104.
- Zoback, M.D. and J.C. Zinke, 2002, Production-induced normal faulting in the Valhall and Ekofisk oil fields: Pure and Applied Geophysics, **159**, 403-420.
- Zoback, M.D., 2007, Reservoir Geomechanics: Cambridge University Press.
- Zhu L.P. and D.V. Helmberger, 1996, Advancement in source estimation techniques using broadband regional seismograms: Bulletin of the Seismological Society of America, **86**, 1634-1641.

Table 1. Recovered focal mechanisms in the synthetic tests for different hypocenters and faulting types. The true focal mechanisms are listed in the row indicated by REF. Rows D1, D2 and D3 list the events at 1000 m, 1200 m, and 1700 m in depth, respectively.



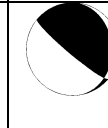
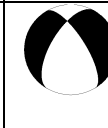




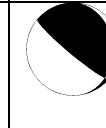


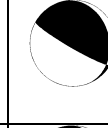
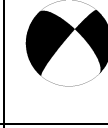



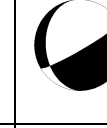
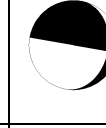


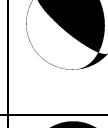
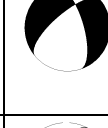

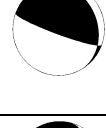


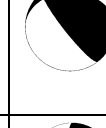
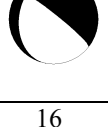

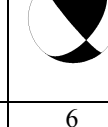
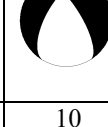
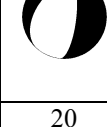
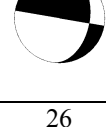
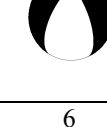

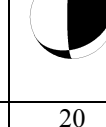
	E1			E2			E3		
	M1	M2	M3	M1	M2	M3	M1	M2	M3
REF									
D1									
D2									
D3									
$\Delta\phi^\circ$	16	23	6	10	20	26	6	14	20
$\Delta\delta^\circ$	20	3	3	13	6	6	6	10	3
$\Delta\lambda^\circ$	3	10	13	3	27	10	16	8	18

Table 2. Recovered focal mechanisms in the synthetic tests for different faulting types using the deep borehole network. The true focal mechanisms are listed in the row indicated by REF. The synthetic events at two different hypocenters are tested (Figure 2).

	E4 (D=1 km)			E5 (D=1.4 km)		
	M1	M2	M3	M1	M2	M3
REF						
Best Sol.						
$\Delta\phi^\circ$	10	50	20	30	10	30
$\Delta\delta^\circ$	10	10	40	10	10	0
$\Delta\lambda^\circ$	10	10	0	30	10	30

Table 3. One dimensional attenuation model used for the DWN waveform modeling. The attenuation affects the waveform amplitudes and causes waveform dispersion.

<b>Depth (m)</b>	<b>Q<sub>p</sub></b>	<b>Q<sub>s</sub></b>
0 – 60	30	20
60 – 110	40	20
110 – 160	60	30
160 – 264	80	40
264 – 470	100	50
470 – 1090	200	100
1090 – bot.	300	150

## Figure Captions

Figure 1. Distributions of near-surface stations and located events. a) Map view of the studied field. The blue hexagons (E1, E2 and E3) are the epicenters of synthetic events and the green triangles (VA11, VA21, VA31, VA41 and VA51) are the five near-surface stations. These stations are located in shallow boreholes 150 m below the surface to increase the signal-to-noise ratio (SNR). The black lines are the identified faults. b) Side view of the studied field. Most of the induced microearthquakes are localized around 1 km below the surface.

Figure 2. a) Map view of the borehole network and the microearthquakes located by this network. The yellow diamonds (E4, E5) are the epicenters of synthetic events. The green dots are the surface locations of the five wellbores where receivers are installed. b) Side view of the borehole network and located microearthquakes. The green triangles indicate the borehole stations. The vertical distance between two consecutive receivers in a monitoring well ranges from ~20 m to ~70 m.

Figure 3. The vertical components of seismograms of a typical event recorded by the surface network and the corresponding spectrograms. The filtered seismograms (3~9 Hz) are in the left column; the original seismograms are in the middle; the spectrograms of the original seismograms are at the right. The zero time is the origin time of the event.

Figure 4. The vertical components of seismograms of a typical event recorded by the borehole network. The filtered seismograms (15~35 Hz) are in the left column; the original seismograms



are in the middle; the spectrograms of the original seismograms are at the right. The zero time is the origin time of the event.

Figure 5. P- (right) and S-wave (left) velocity perturbations for the synthetic tests. The reference velocities, plotted with the bold black line, are used for calculating the Green's functions. The perturbed velocities (colored lines) are used to generate the synthetic data for each station.

Figure 6. Moveouts of the P- and S-waves with distance. The source is at 900 m in depth, and the receivers (vertical components) are at 150 m in depth. The green lines indicate the first P- and S-wave arrivals obtained from finite-difference travel time calculation method based on the eikonal equation.

Figure 7. Comparisons between modeled waveforms (red) and synthetic data (blue) at 5 stations with perturbed velocity model. From top to bottom, waveforms from the vertical components at stations 1 through 5, respectively, are shown. The waveforms are filtered between 3 and 9 Hz. The left column shows P-waves and right column shows S-waves. The green lines indicate the first P arrival times. For P-waves, zero time means the origin time, and for S-waves, zero time means the S-wave arrival time predicted by the calculated traveltime. The "shift" in the title of each subplot indicates the time shifted in the data to align with the synthetic waveforms. In the left column, the "+" or "-" signs indicate the first arrival polarities of P-waves in the synthetic data and those in the modeled data, respectively. In the right column, the number to the left of the

slash denotes the S/P amplitude ratio for the synthetic data, and the number to the right of the slash denotes the ratio for the modeled waveform.

Figure 8. Comparisons between modeled waveforms (red) and synthetic data (blue) at nine borehole stations with the perturbed velocity model. In this test, nine vertical components in borehole YA, YB, YC and YD are used. The waveforms are filtered between 15 and 35 Hz. The true mechanism is  $(210^\circ, 50^\circ, -40^\circ)$ , and the best recovered one is  $(240^\circ, 60^\circ, -10^\circ)$  in comparison.

Figure 9. Focal mechanism solutions for a typical event determined by the shallow network. The one at the bottom right (#1) is the best solution with maximum objective function value. The epicenter is shifted northward (Y) by about 750 m, eastward (X) by about 300 m and the depth is shifted 50 m deeper compared to the original hypocenter. The shift in epicenter may be biased by inaccuracy in the velocity model and by only using the vertical components. The shift can compensate the phase difference between the modeled seismograms and the real seismograms.

Figure 10. Comparison between the modeled waveforms (red) and the real data (blue) at 5 surface network stations for a typical event. For P-waves, zero time means the origin time, and for S-waves, zero time means the S-wave arrival time predicted by the calculated travel time.

Figure 11. Comparison between the modeled waveforms (red) and the real data (blue) from the borehole network. 11 stations and 5 first P-wave arrival polarities are used in this determination. For P-waves, zero time means the origin time, and for S-waves, zero time means the S-wave arrival time predicted by the calculated travel time.

Figure 12. a) Focal mechanisms of the 40 events inverted in this study from both the surface and borehole networks. The background color in the map indicates the local change in surface elevation with a maximum difference of about 10 m. Different focal mechanisms are grouped in several colors. The events and their focal mechanisms determined by the surface network are plotted in the outer perimeter, while the ones by the borehole network are plotted in the inner ring. b) Side view of the depth distribution and focal mechanisms of the studied events. Because only vertical components are used in our focal mechanism determination, our results are not very sensitive to epicenter shifting. Therefore, the event epicenters shown in a) are from the travel time location and the event depths in b) are from the waveform matching process.

Figures

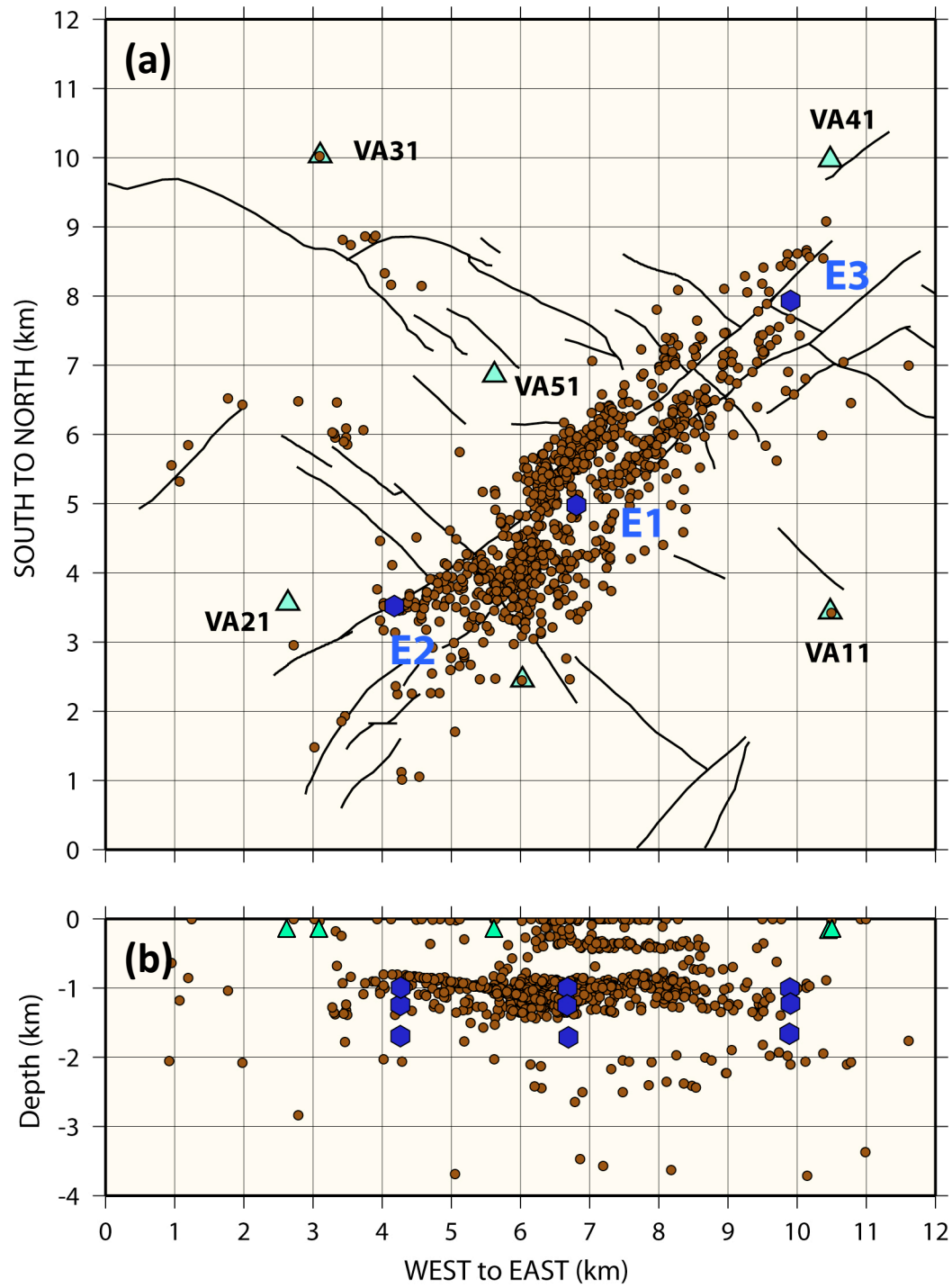


Figure 1.

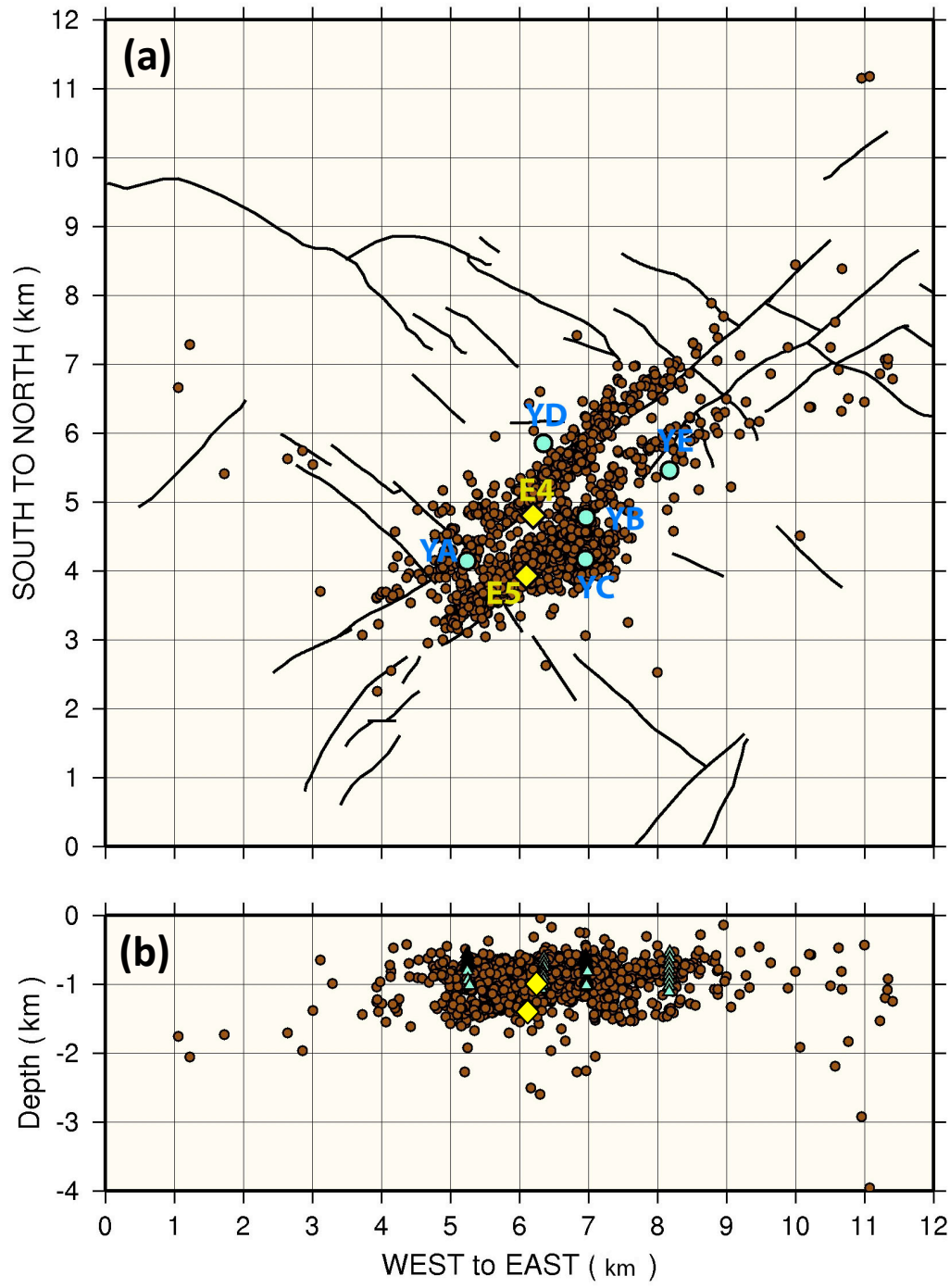


Figure 2.

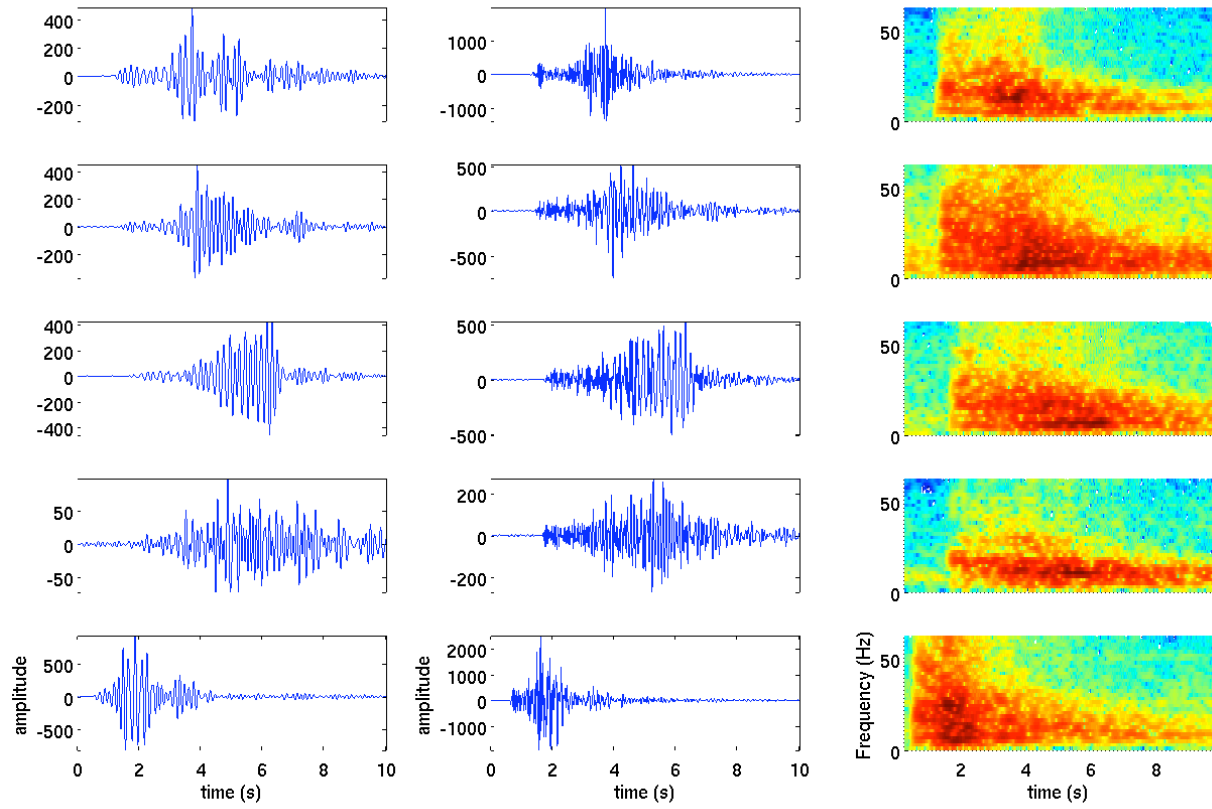


Figure 3.

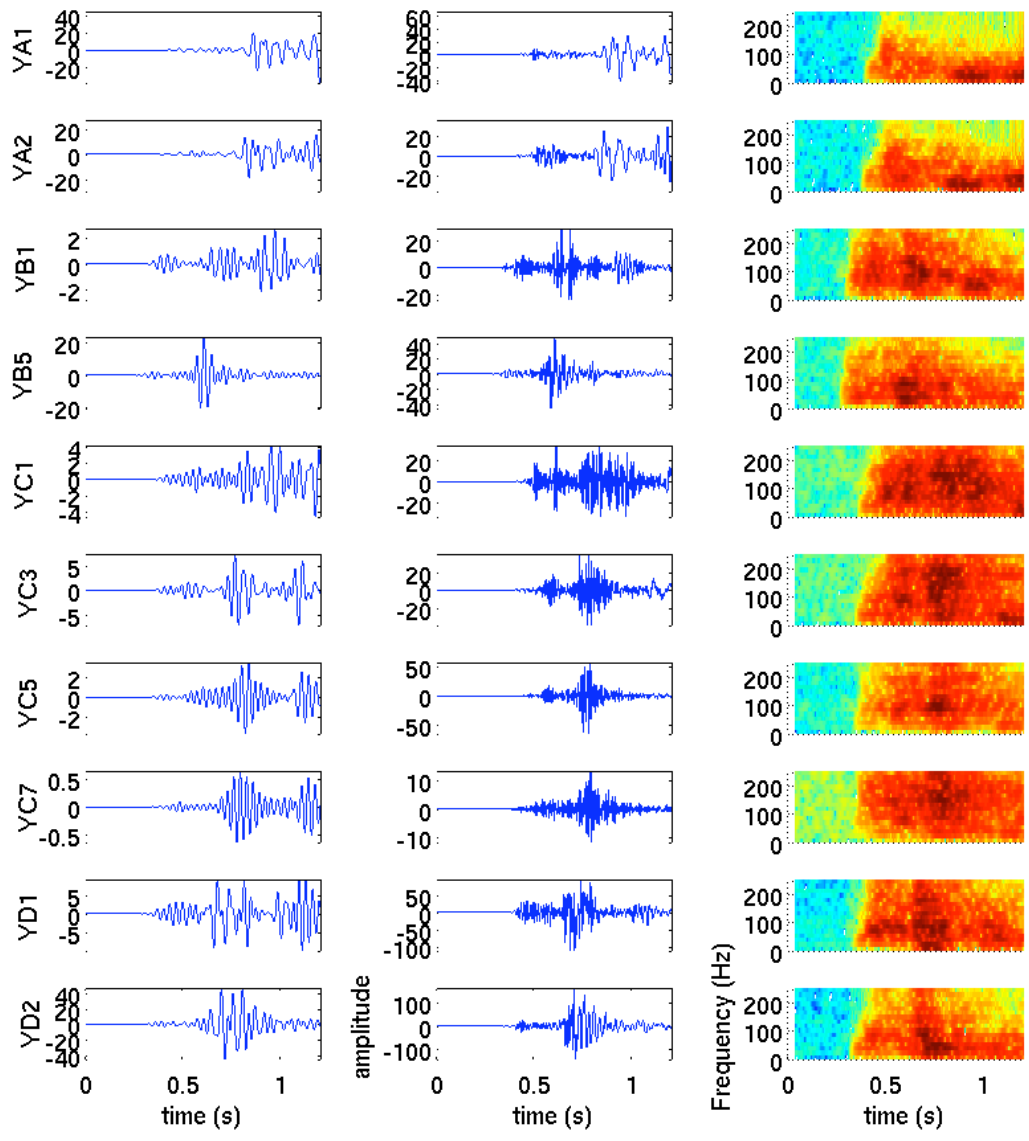


Figure 4.

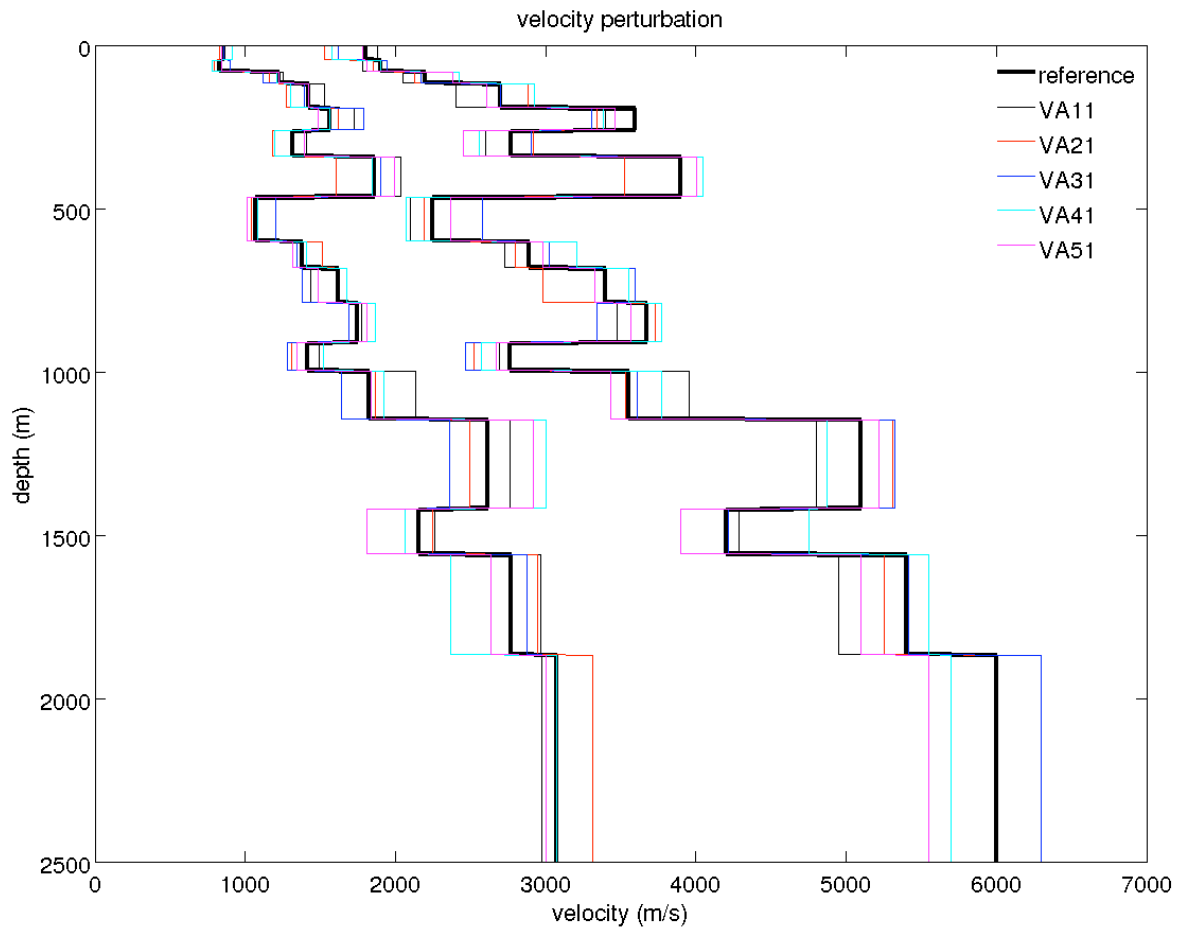


Figure 5.



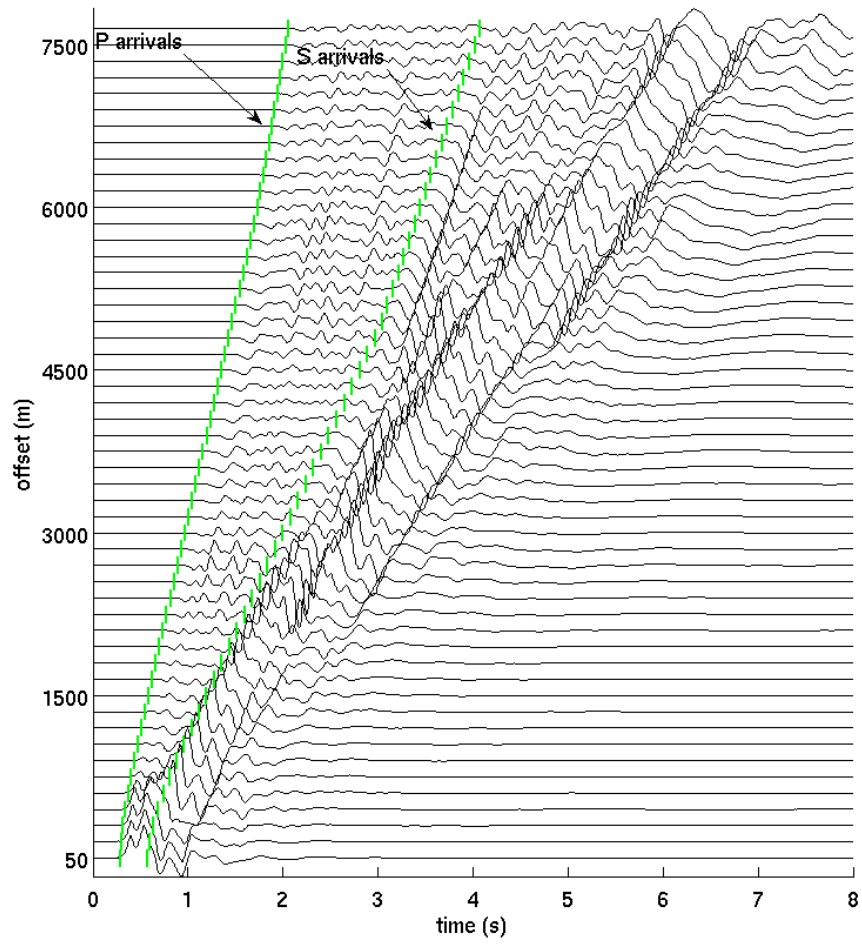


Figure 6.

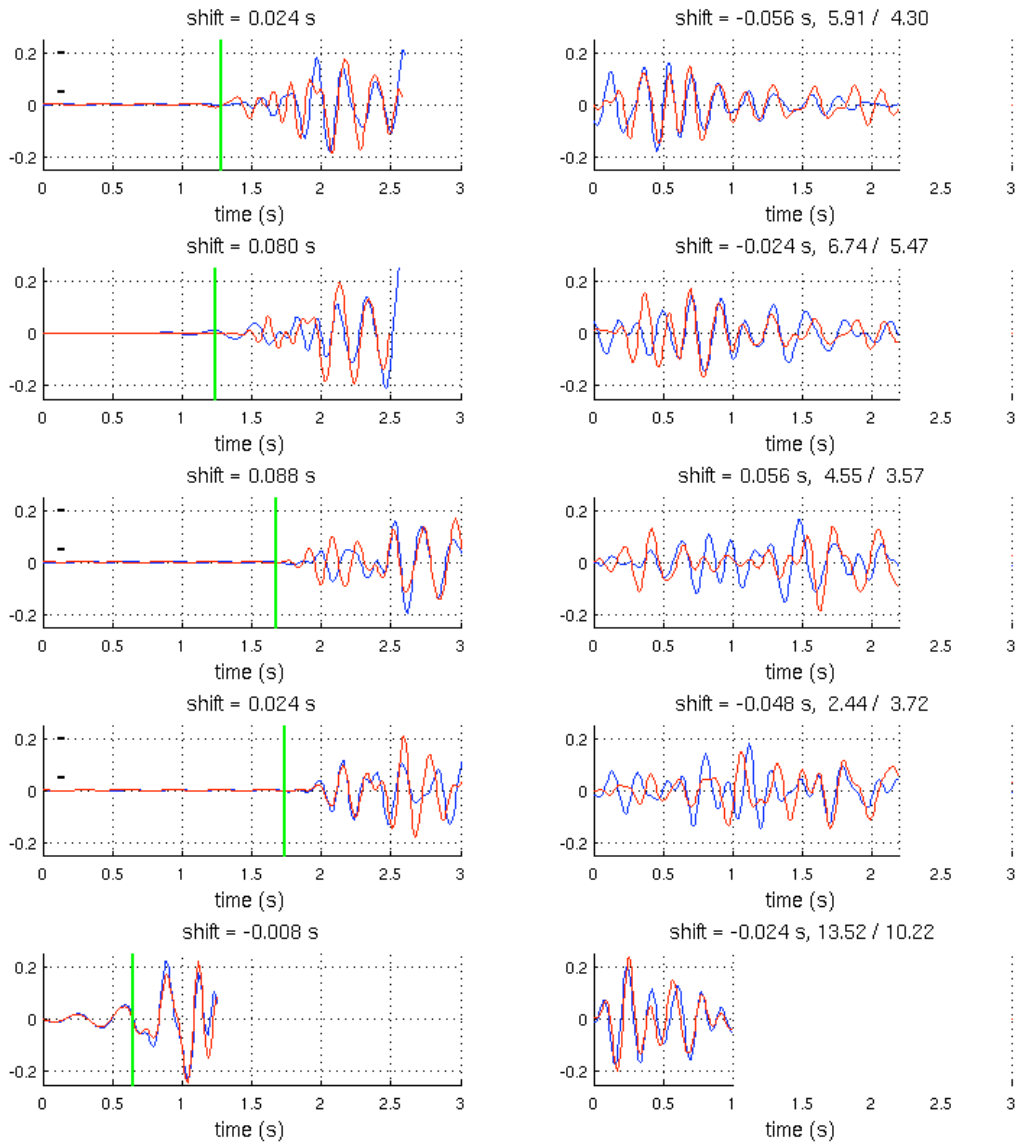


Figure 7.

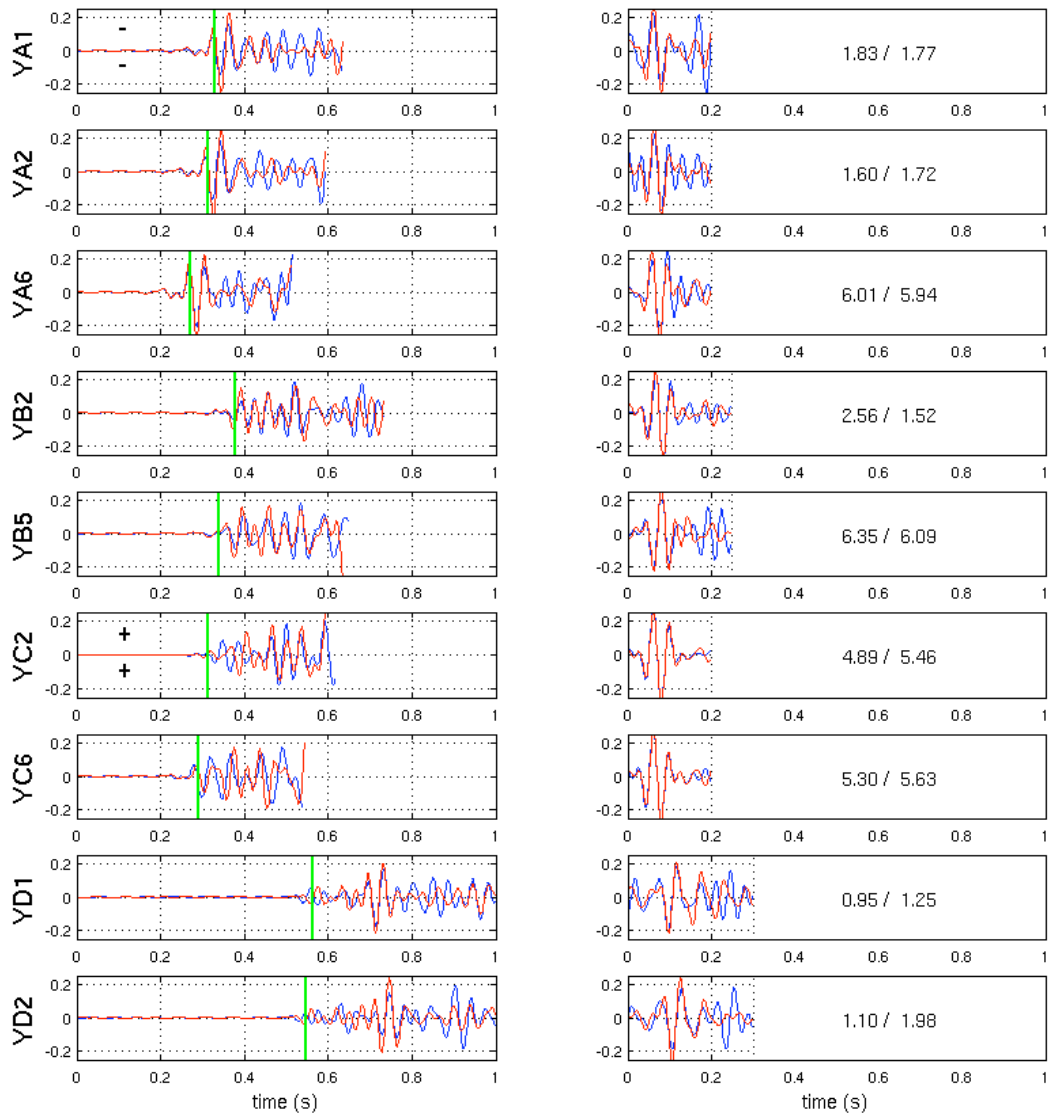
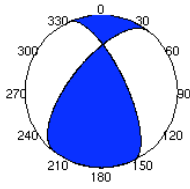
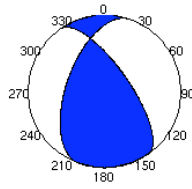


Figure 8.

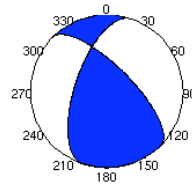
9. str=335°;218°, dip=60°;52°, rake=45°;141° X=150 m, Y=600 m, depth= 50 m



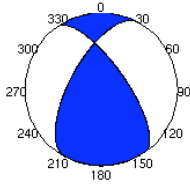
8. str=325°;199°, dip=60°;45°, rake=55°;135° X=150 m, Y=900 m, depth= 50 m



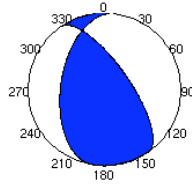
7. str=315°;198°, dip=60°;52°, rake=45°;141° X=300 m, Y=900 m, depth= 50 m



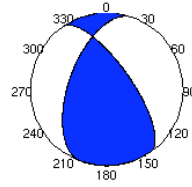
6. str=325°;208°, dip=60°;52°, rake=45°;141° X=150 m, Y=900 m, depth= 50 m



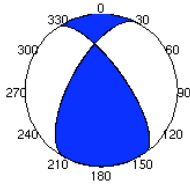
5. str=325°;188°, dip=60°;38°, rake=65°;126° X=300 m, Y=750 m, depth= 50 m



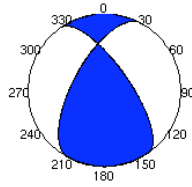
4. str=325°;199°, dip=60°;45°, rake=55°;135° X=150 m, Y=750 m, depth= 50 m



3. str=325°;208°, dip=60°;52°, rake=45°;141° X=300 m, Y=750 m, depth= 50 m



2. str=325°;208°, dip=60°;52°, rake=45°;141° X=150 m, Y=750 m, depth= 50 m



1. str=325°;199°, dip=60°;45°, rake=55°;135° X=300 m, Y=750 m, depth= 50 m

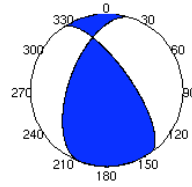


Figure 9.

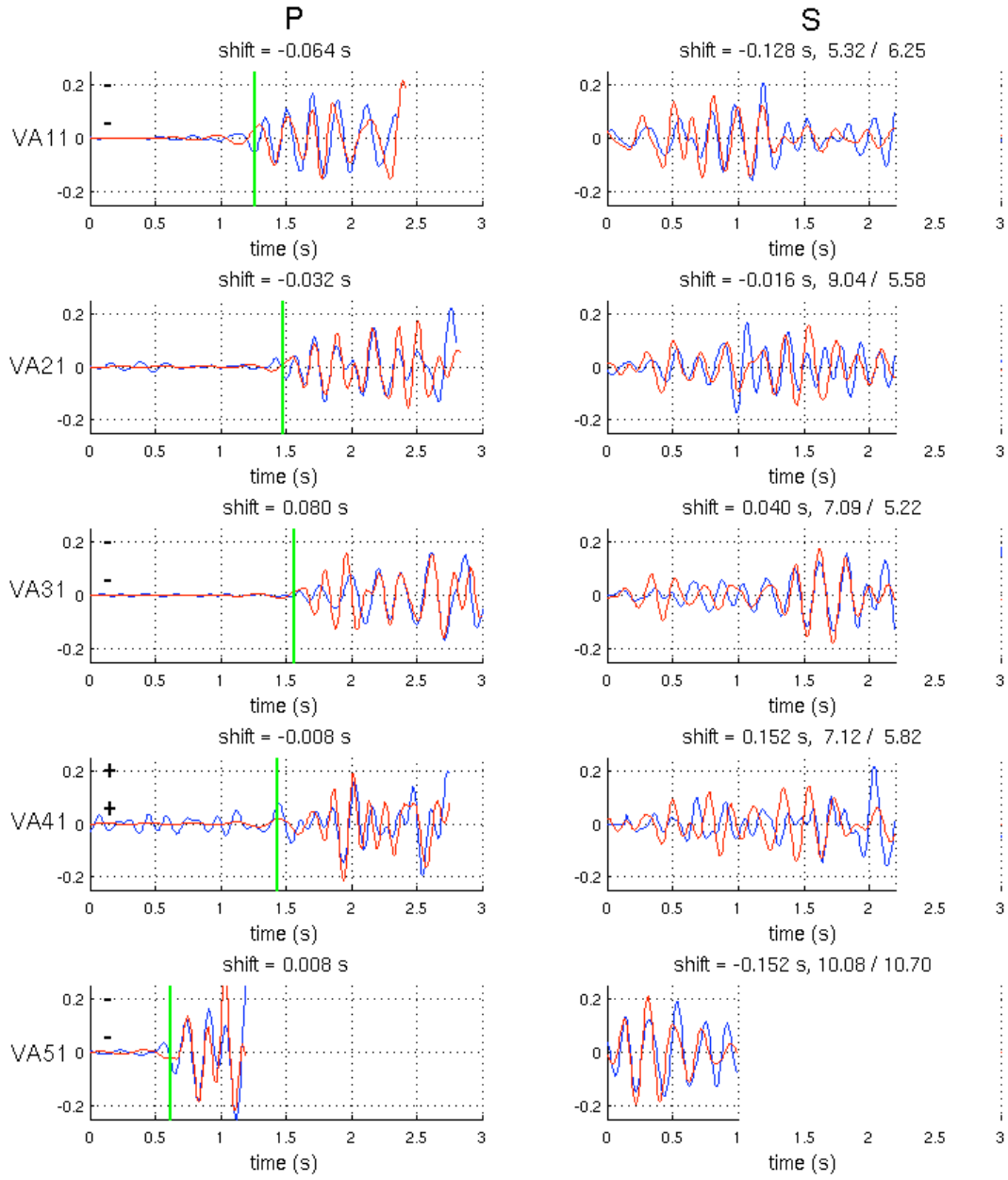


Figure 10.

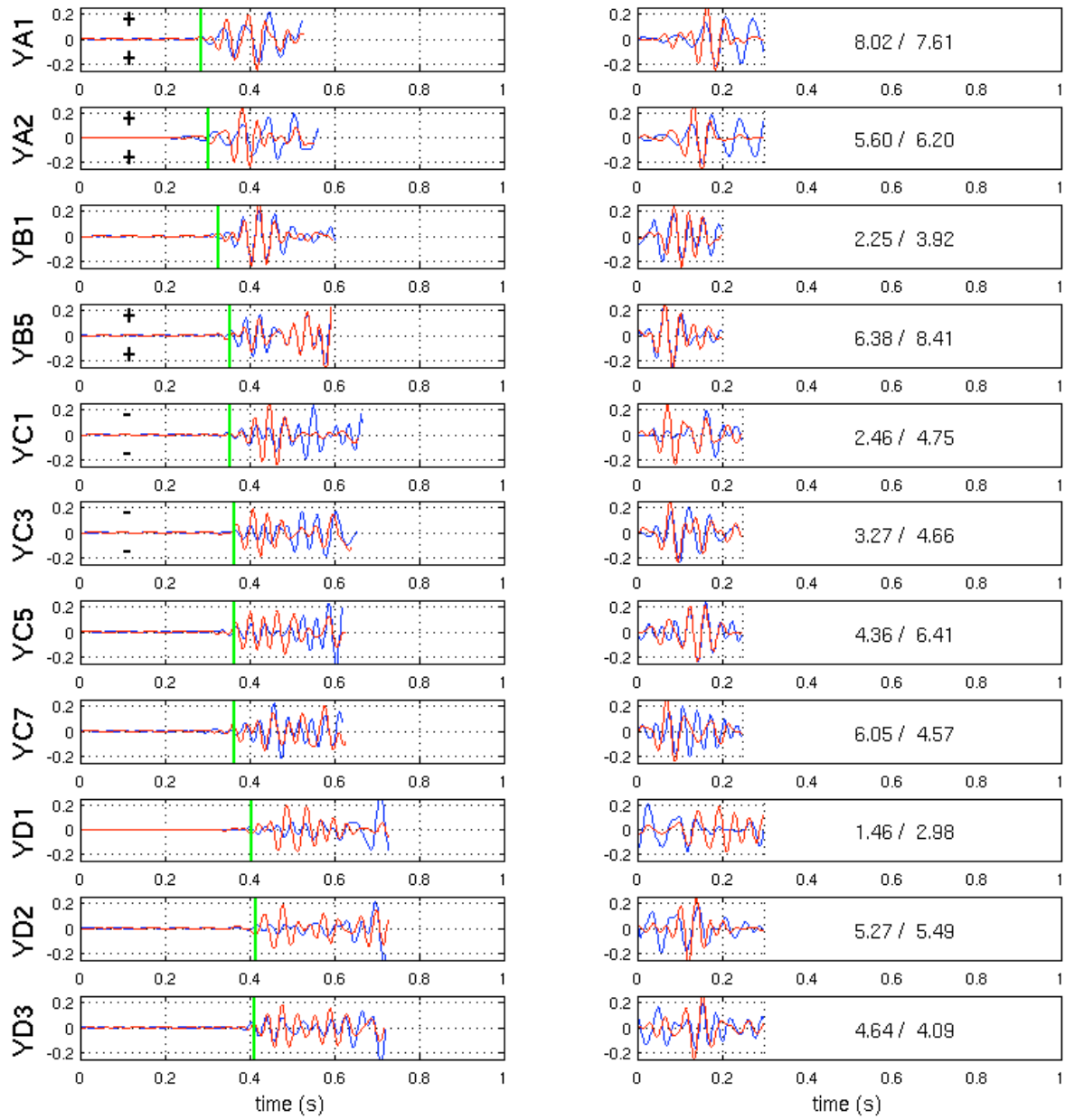


Figure 11.

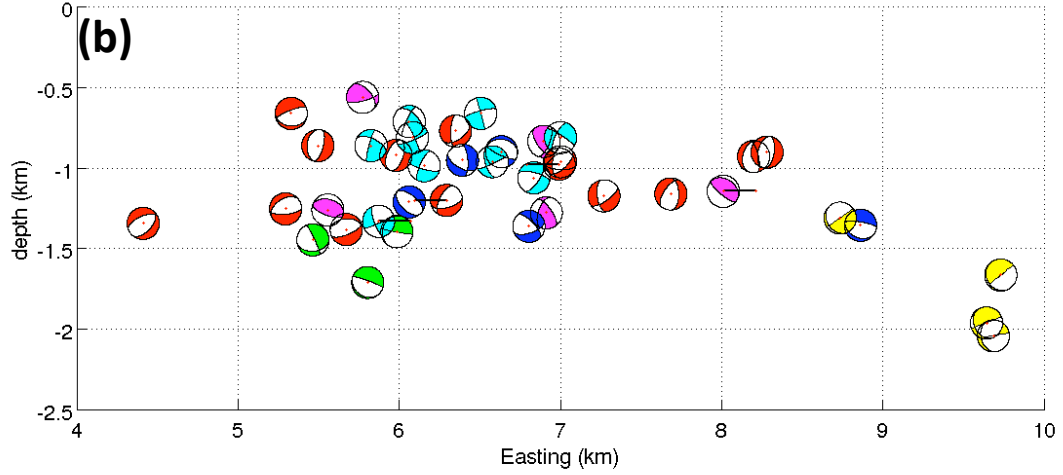
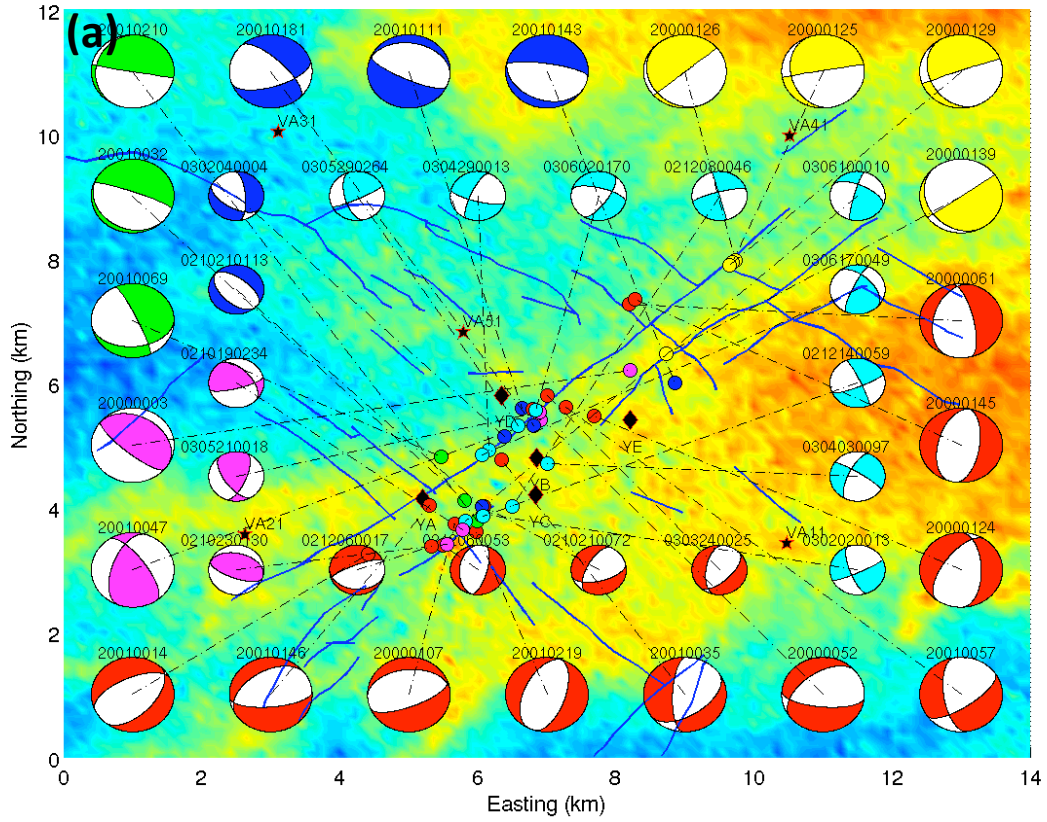


Figure 12.

## Appendix: Green's Functions Calculation for the Deep Borehole Network

The reflectivity method used in the discrete wavenumber waveform modeling of Bouchon (2003) was originally developed in global seismology where sources are located underground and receivers are at the surface or near the surface. For the surveys using borehole receivers, however, the receivers can be located deeper than the source; thus the original reflectivity method needs to be revised and calculations in the reflectivity method need to be modified for this configuration. We followed the symbols and definitions used in the paper by Muller (1985) on the reflectivity method and only show the key modified equations. Figure A1 shows the diagram for borehole receiver configuration.

The source and receivers are required to be located at the interface between two identical layers in the implementation (Bouchon, 2003). The position of the source and receiver can be anywhere within a layer, however, an artificial splitting of the layer is applied at the depth of the receiver or the source, i.e., splitting the layer into two identical layers with an interface at the depth of the source or receiver. The reflectivity method is easier to apply in this way. After the splitting, the source is located at the bottom of layer  $j$ , and the receiver is located at the top of layer  $m$  for the shallower-source-deeper-receiver situation.

In the following derivation, we use the P-SV system. For the SH system, the matrices and vectors are replaced with scalars. The overall amplitude vector  $V_{1,2}^D$  for the down-going waves at the source depth is:

$$V_{1,2}^D = \begin{pmatrix} A_{1,2} \\ C_{1,2} \end{pmatrix} = (S_{1,2}^d + R^+ R^- S_{1,2}^d + R^+ R^- R^+ R^- S_{1,2}^d + \dots) + (R^+ S_{1,2}^u + R^+ R^- R^+ S_{1,2}^u + R^+ R^- R^+ R^- R^+ S_{1,2}^u + \dots) \quad (\text{A1})$$

$$= (I - R^+ R^-)^{-1} (S_{1,2}^d + R^+ S_{1,2}^u)$$



where  $R^+$  and  $R^-$  are the reflectivities illustrated in Figure A1;  $S_{1,2}^d$  and  $S_{1,2}^u$  are the source amplitude vectors;  $I$  is the identity matrix.  $V_{1,2}^D$  takes all the reflections from the lower layers (first bracket) and the upper layers (second bracket) into consideration and, therefore is the amplitudes of the *overall* down-going P- and SV-waves at the source depth. After the *overall* down-going amplitudes are obtained at the source level, we need to propagate them down through the layers between the source and receiver by the overall down-going transmissivity matrix:

$$TT^D = F_{m-1}F_{m-2}\dots F_{j+1}F_j \quad (\text{A2})$$

where  $F_k$  characterizes the amplitude change through layer  $k$  and through the bottom interface of layer  $k$ . Note that for layer  $j$  there is no phase shifting through the phase matrix  $E_j$  in  $F_j$ , as the source is already located at the bottom of layer  $j$  after the artificial splitting. The overall down-going amplitudes at the receiver then are:

$$V_{1,2}^{D,R} = \begin{pmatrix} A_{1,2}^R \\ C_{1,2}^R \end{pmatrix} = TT^D V_{1,2}^D \quad (\text{A3})$$

and the overall amplitudes of the up-going waves at the receiver are related to the amplitudes of the down-going waves by:

$$V_{1,2}^{U,R} = \begin{pmatrix} B_{1,2}^R \\ D_{1,2}^R \end{pmatrix} = MT_m V_{1,2}^{D,R} \quad (\text{A4})$$

where  $MT_m$  is the local reflectivity matrix at the top of layer  $m$ . Combining the amplitudes  $V_{1,2}^{U,R}$  and  $V_{1,2}^{D,R}$  with the Green's functions calculated by the discrete wavenumber method (Bouchon, 2003) and integrating in the wavenumber and frequency domain, we can then obtain the analytic solution in a stratified medium where the receiver is deeper than the source.

**Appendix Figure Caption**

Figure A1. Diagram of the reflectivity method for the deep borehole receiver configuration.

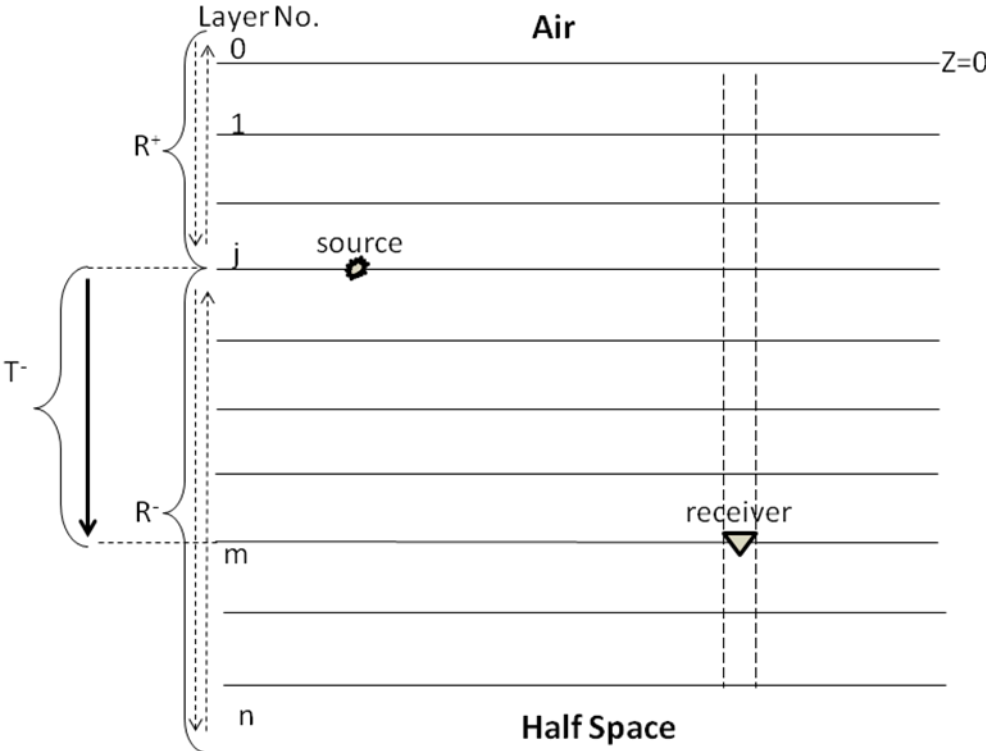


Figure A1.